A statistical study of F-region 3.2-m-scale field-aligned irregularities (FAIs) occurrence and vertical plasma drift over Hainan: solar activity, season and magnetic activity dependences

Han Jin[1], Shasha Zou[2], Chunxiao Yan[1,3], Guotao Yang[1], Gang Chen[1,3], Shaodong Zhang[3], Jingye Yan[1], Shan Yi[3], Zhihua Wang[3]

[1] State Key Laboratory of Space Weather, National Space Science Center, Chinese Academy of Sciences, Beijing, China

[2] University of Michigan, Ann Arbor, MI, United States

[3] Wuhan University, Electric Information School, Hubei, China

Corresponding author: G. Chen g.chen@whu.edu.cn and H. Jin jinhan@nssc.ac.cn

Key Points

- Solar flux and seasonal variations of FAIs occurrence rate are controlled by the vertical drift velocity pattern
- Abnormally low post-midnight FAIs occurrence rate in June solstice under low solar flux is attributed to the inactive ITCZ around 110° E
- Enhanced geomagnetic activity tends to weaken the upward drift velocity and suppress the FAIs generation over Hainan in the dusk side

Abstract

This is the author manuscript accepted for publication and has undergone full peer review but has not been through the copyediting, typesetting, pagination and proofreading process, which may lead to differences between this version and the Version of Record. Please cite this article as doi: 10.1029/2020JA028932.

The dependences of the nighttime low-latitude F-region 3.2-m-scale field-aligned irregularities (FAIs) occurrence and vertical drift on solar activity, season and magnetic activity during 2014-2017 are studied by using the coherent scatter radar located at Fuke (19.5°N, 109.1°E), and a nearby Digisonde at Sanya (18.4°N, 109.6°E), Hainan Island, China. The post-sunset FAIs occurrence and vertical drift are closely related and modulated by the solar activity, especially for equinox. Utilizing the day-to-day comparison analysis, the threshold of the peak V_z for the definitive post-sunset FAIs generation during equinox was ~30 m/s. The post-midnight FAIs occurrence in June solstice did not increase with the decreasing solar activity and is different from the nearby longitude 100 °E reported by other studies. This difference is suggested to be due to the different Intertropical Convergence Zone activity between the two longitudes and reveals the highly localized and dynamic nature of irregularities, which clearly highlights the related challenges of space weather forecast. The SYM-H and AE indices are used as indicators of the geomagnetic activity level, and the statistical results show that enhanced geomagnetic activity appears to weaken the evening V_z and thus suppress the subsequent FAIs generation during the post-sunset period. Westward substorm-related over-shielding electric field and/or disturbance dynamo electric field in the dusk side are suggested to play a role in the FAIs suppression during geomagnetic disturbances. This study contributes to the limited available statistical results in the Asian sector and is valuable for the holistic understanding of the global small-scale FAIs occurrence pattern.

1 Introduction

Equatorial plasma bubbles (EPBs) are plasma density depletions, which initiate in the equatorial or low-latitude F-region ionosphere bottom side and grow to the topside in the form of magnetic

field-aligned structures. They usually occur after local sunset, when the conductivity at the E-region ionosphere becomes negligible that creates a favorable condition for the EPBs development. Density gradient at the EPBs boundaries may cascade into irregularities with a wide range of scale sizes, ranging from 10^{-2} to 10^{5} m (Kelley, 1989), and thus could affect the radio waves spanning a wide frequency range. Different terms have been used to characterize the F-region irregularities observed by different instruments, such as "spread F" in ionosonde observation, "plumes" of field-aligned irregularities (FAIs) in radar backscatter observations, density "depletions" or "bite-outs" in in-situ satellite observations and so on. The dynamics and characteristics of the ionospheric irregularities have been extensively studied for many decades due to its adverse impact on radio communication and navigation systems between satellites and ground. Studies have been carried out to investigate the occurrence characteristics of the F-region irregularities by using data from various equipment, such as coherent and incoherent scatter radars, ionosonde, low-earth orbiting (LEO) satellite, radio scintillation detector and airglow imager (e.g., Li et al., 2009; Smith et al., 2016; Shi et al., 2011; Huang et al., 2001; Burke et al., 2004a, 2004b; Okoh et al., 2017).

It has been widely accepted that EPBs are generated by the generalized Rayleigh-Taylor (R-T) instabilities (Ott, 1978) starting at the bottomside of the F layer. In the post-sunset sector, the F layer can be uplifted by the enhanced eastward electric field (known as pre-reversal enhancement of eastward zonal electric field, i.e., PRE) to higher altitude, where the ion-neutral collision frequency v_{in} is much lower and thus favors the growth of R-T instability. The magnitude of PRE is a crucial parameter to modulate the EPBs generation. A threshold value of vertical drift in the post-sunset sector is suggested to be necessary for the EPBs generation, and the occurrence

rate of EPBs increases with the magnitude of the PRE (Huang, 2018a and references therein). Therefore, it is necessary to take the vertical plasma drift effects on EPBs development into consideration when discussing the seasonal, solar flux and magnetic activity variations of the EPBs occurrence.

The EPBs occurrence displays considerable seasonal and longitudinal (e.g., Huang et al., 2001; Burke et al., 2004a, 2004b; Su et al., 2008; Carter et al., 2013; Wan et al., 2018; Yizengaw and Groves, 2018) variations. Tsunoda (1985) suggested that the maxima in EPBs activity occur during the period when the sunset terminator is almost aligned with the geomagnetic flux tubes. The nearly simultaneous sunsets at the conjugate E layers cause a speedy decrease of the integrated E-region Pedersen conductivity $\sum_P^E$, and hence result in the rapid growth of R-T instability. For longitudes where the magnetic declination is close to 0°, the occurrence of EPBs should maximize near equinoxes, when the sunset terminator closely aligns with the geomagnetic field lines. In contrast, the maximum of plasma bubble occurrence shifts to June (December) solstice in longitudes of eastward (westward) magnetic declination. The occurrence of EPBs is also affected by solar and geomagnetic activities. It has been known that the formation of EPBs is more prominent during solar maximum than that during solar minimum as inferred from the scintillation observations, due to the enhanced background ionization density and thus the conductance term of the R-T instability growth rate (e.g., Basu et al., 1998, 2002). The effect of geomagnetic disturbances on the equatorial EPBs occurrence has been studied a lot in recent years and has not been fully understood due to its complexity, i.e. suppression or excitation of the EPBs formation at different local times (e.g., Martinis et al., 2005; Tulasi Ram et al., 2008; Abdu, 2012 and references therein; Aa et al., 2018, 2019; Jin et al., 2018). The zonal

electric field can be modified by two important drivers during geomagnetic disturbances. The first one is prompt penetration electric field (PPEF) from high latitude to low latitude (Nishida, 1968). The PPEF penetration to equatorial/low-latitude ionosphere can be established very quick, usually right after sudden and large southward (northward) turning of interplanetary magnetic field (IMF) Bz or geomagnetic activities, such as substorms (e.g. Kikuchi et al., 2003; Hashimoto et al., 2011). The other driver is the global thermospheric wind modulated disturbance dynamo electric field (DDEF) (Blanc and Richmond, 1980), which occurs with a couple of hours delay from the commencement of geomagnetic disturbances, usually during the recovery phase of the storm. The under-shielding PPEF is eastward (westward) on the day (night) side, while the over-shielding electric field and DDEF have opposite polarity of the under-shielding PPEF. Thus, the effect of these electric fields on the EPBs occurrence differs in the post-sunset and post-midnight sectors. Consequently, the response of EPBs occurrence to geomagnetic disturbances depends on the interplay among these electric field perturbations. The perturbation of vertical plasma drift can serve as the direct evidence of storm-time perturbation electric field's modulation on equatorial and low-latitude ionosphere by modifying the vertical plasma motion, so it is necessary to consider the relationship and establish connection between storm-time vertical plasma drift pattern and EPBs development response to geomagnetic activities.

There are a few statistical studies about low-latitude irregularities in the East Asia region in the past years, and the results have revealed some characteristics about the occurrence of low-latitude irregularities. For example, using data from Digisonde and ionospheric scintillation monitor, Shi et al. (2011) analyzed the relationship between strong range spread F and

scintillations over Hainan in the period of declining solar cycle 23 from 2003 to 2007 and found that both the range spread F and the scintillation occurrences decreased with decreasing solar activity. Based on the total electron content (TEC) observations, Li et al. (2009) studied the suppression effect of magnetic disturbance on the EPBs occurrence in East Asia for the period of 2001-2004, i.e., during the peak of solar cycle 23. Moreover, Kumar et al. (2016) analyzed data from 12 GPS receivers in the Hong Kong region from 2001 to 2012 to study the dependence of EPBs occurrence on solar activity, and the magnetic activity effect on EPBs occurrence was discussed in terms of two cases of magnetic storms, i.e., one triggered by PPEF and another one suppressed by DDEF. VHF radars have been used for detecting backscatter echoes caused by the Bragg scatter from FAIs with a scale size of half of the radar wavelength. For instance, Xie et al. (2018) investigated the occurrences of ionospheric E-region, valley and F-region FAIs in the post-sunset period by using the observations from the low-latitude five-beam Sanya, Hainan Island of China (18.4°N, 109.6°E) VHF radar and Sanya Digisonde during equinoctial months of 2012-2016. Hu et al. (2020) studied the statistical characteristics and correlation of equinoctial bottom-type and plume irregularities over Sanya during equinox of 2011-2018 and found that bottom-type and plume irregularities showed opposite correlation with F-layer virtual height. Statistical studies of the EPBs occurrence during the moderate solar activity years 2011-2012 at nearby longitude have been conducted by Ajith el al. (2015) using data from multi-beam Equatorial Atmosphere Radar (EAR) at Kototabang (0.2°S, 100.3°E), Indonesia. Their results showed that the evolving-type and drifting-in EPBs exhibit predominance during the post-sunset period in equinoxes and December solstice and the evolving-type EPBs displayed a secondary peak around midnight (2300-0100LT) which were caused by the EPBs development during post-midnight hours of June solstices.

In this study, a comprehensive study of the dependences of low-latitude 3.2-m scale FAIs occurrence and vertical plasma drift on solar activity, season, and magnetic activity during the years of 2014-2017, i.e., the declining phase of solar cycle 24, is performed by using data from the coherent scatter radar located at Fuke, Hainan island, China and a nearby Digisonde at Sanya, Hainan island, China. Simultaneous observations from two nearby instruments allowed us to estimate the role of nighttime vertical plasma drift variation on the FAIs occurrence and analyze their response to solar and magnetic activities variations. Section 2 describes the measurements and the method of our analysis in this study. We present the statistical results of the FAIs occurrence and vertical plasma drift dependence on solar activity, season and magnetic activity and include detailed discussion in section 3. Section 4 summarizes our results and conclusions. This study improves our understanding of the relationship between low-latitude FAIs occurrence and vertical plasma drift under both quiet and disturbed conditions in the eastern Asian sector.

2 Data and Method

The Hainan COherent scatter Phased Array Radar (HCOPAR), located at Fuke, Hainan Island of China (19.5°N, 109.1°E; magnetic latitude 9.58°N), has been continuously operated to observe the F-region FAIs since February 2014. Its operating frequency is 47 MHz, so the radar is sensitive to 3.2-m-scale FAIs in the low-latitude ionosphere. Figure 1 displays the locations of the two instruments (marked with a black star for Fuke and a black triangle for Sanya) and the beam directions (seven white fans) of the HCOPAR. The HCOPAR can steer its beam to scan within $\pm$22.5° in azimuth around the geographic north, with each scan separated by 7.5°. The seven radar beams from the easternmost to the westernmost direction are labeled with Beam 1 to

7, respectively, and one complete azimuthal scan from Beam 1 to Beam 7 takes about 2 mins. The range resolution of the HCOPAR is 0.711 km. It is one of the most important radio systems of the Chinese Meridian Project (Wang, 2010). A detailed description of the HCOPAR can be found in Chen et al. (2017) and Jin et al. (2018). The filled contours in Figure 1 show the geomagnetic field declination near the radar site. The red dashed line shows the solar terminator at the sunset time over Fuke at the March equinox in 2014. The F-region observation obtained by seven beams of the HCOPAR during the period from 2014 to 2017 is used for this statistical study.

Figure 2 displays an example of the FAIs measurement and our automated method of FAIs identification. Figure 2(a) shows the signal-to-noise ratio (SNR) plot of coherently backscattered echoes from Beam 4 of the HCOPAR as a function of altitude versus universal time on 24 February 2014. The occurrence of FAIs can be identified by echoes with SNR larger than 5 dB by using time-range bins of 2 mins and 0.711 km as depicted in Figure 2(b). Yellow/blue indicates the occurrence/non-occurrence of FAIs. The threshold of SNR to identify FAIs event varies a lot among different radars (i.e., Smith et al., 2016, Zhan et al., 2018). In the course of statistical analysis, we have carried out sensitivity studies by testing a range of dB values and found that the threshold of 5 dB is not only a good criterion for FAIs event identification but also useful for excluding clutter echoes. Figure 2(c) shows the universal time variation of the FAIs index, defined by the averaged SNR of the echoes from altitude 200 km to ~572 km (maximum detectable altitude of the HCOPAR). The FAIs index not only reveals the occurrence of FAIs in echo intensity but also in altitude. In other words, the larger value of the FAIs index represents stronger FAIs and/or larger coverage of the FAIs altitude. The FAIs index can also be used for

the FAIs identification at each universal time bin by using the criterion of FAIs index ≥1. If there were FAIs emerging in at least one of the seven beams of the HCOPAR and the FAIs remained in the field of view (FoV) of the HCOPAR for more than 15 mins, then the corresponding day was recognized as a FAIs event day.

The vertical plasma drift used in this study was obtained from a nearby Digisonde Portable Sounder (DPS-4D; Reinisch et al., 2009) at Sanya for the same period. The Sanya Digisonde is operated under drift-mode to measure the apparent mean velocities of plasma structures in the ionospheric F-region. To investigate the relationship between the vertical drift velocity and FAIs occurrence, daily measurements from 06:00 UT to 18:00 UT were analyzed in this study. The time resolutions of F-region measurement are 15 mins for 06:00-11:51 UT and 7 or 8 mins for 11:58-18:00 UT. Bertoni et al. (2006) have compared the ionospheric vertical drift velocities derived from Digisonde measurement under drift-mode with those calculated with dhF_{80}/dt and derived from incoherent scatter radar measurement at Jicamarca Radio Observatory. They found good agreement in these datasets when the bottom height of F-layer is around and above 300 km where photo-chemistry/recombination effects become less dominant. During the nighttime period, the operating frequency of Sanya Digisonde under drift-mode is usually more than ~7 MHz, ensuring that the apparent vertical drift velocities measured by Sanya Digisonde are mostly from near and above 300 km and are close to the practical vertical plasma drift. In order to reduce the effect of recombination process on altering the nighttime F layer height, measurements from low altitudes have been eliminated to reduce measurement error as possible. Considering the PRE at Hainan usually peaks at around 11:00-12:00 UT, we excluded the

observational days when the data gap in vertical drift velocity during 09:00-13:00 UT exceeds 60 min to ensure the validity of calculating the mean vertical drift and the peak PRE.

3 Results and Discussions

The FAIs index, defined by the averaged SNR of the echoes from altitude 200-572 km, during 10:00 UT-22:00 UT (LT=UT+7.3 hr) from January to December for the period of 2014-2017 is depicted in Figure 3(a)-(d). The lightest color represents data gaps in the HCOPAR observations. The FAIs occurrence can be identified by the FAIs index≥1. It can be seen in Figure 3 that most of the FAIs events started to emerge after 12:00 UT (19:18 LT) and could last for several hours within the FoV of the HCOPAR, and some of them can persist into the post-midnight sector (beyond 16:42 UT).

3.1. Solar Activity and Seasonal Dependences

3.1.1 Quiet-time FAIs Occurrence Climatology

To exclude the magnetic activity effect on FAIs occurrence, Figure 4 depicts the quiet-time (daily mean kp index no exceed 3) monthly occurrence rate of the FAIs over Fuke from 2014 to 2017. The grey bars in Figure 4(a) present the number of days during which the HCOPAR measurements are available and the dark blue bars present the number of days with FAIs event recorded by the HCOPAR for each month. Figure 4(b) presents the normalized occurrence rate of FAIs in each month for 2014-2017. The temporal variation of the daily-averaged F10.7 index for 2014-2017 is also plotted in Figure 4(b). The F10.7 solar index shows the highest level of solar activity in 2014 and keeps decreasing each year, dropping to near solar minimum level by the end of 2017. In this study, we categorized the solar flux activity into three levels, i.e., low

(F10.7<80 sfu), moderate (80≤F10.7<120 sfu) and high (F10.7≥120 sfu) solar activity. It can be seen in Figure 4(b), under high and moderate solar activity conditions, the FAIs occurrence rate showed its maximum around the equinox months (March, April, September and October), second peak around the December solstice (November, December, January and February) and minimum around the June solstice (May to August) as indicated by light blue, orange and light green bars, respectively. Under low solar activity condition, the FAIs occurrence rate in all seasons declined substantially, with a few cases of the FAIs events sporadically occurred in each month. The FAIs occurrence rates in equinox were still slightly higher than other seasons.

To further investigate the FAIs occurrence climatology, Figure 5 shows the color-coded occurrence rate of F-region FAIs observed by the HCOPAR during 2014-2017 as a function of universal time versus altitude for three different seasons and three different solar flux levels. The bin resolution is 2 min in universal time and ~6 km in altitude. The occurrence rate for each universal time versus altitude bin was computed by the following equation

$$\text{FAIs occurrence rate} = \frac{\text{Day numbers with FAIs observed by the HCOPAR}}{\text{Total day numbers with HCOPAR observations}}. \quad (1)$$

Similarly, only observations made on geomagnetic quiet days (daily mean kp index no exceed 3) were used to calculate the occurrence rates. The seasonal and solar cycle variations of FAIs occurrence can also be seen in Figure 5, with the highest occurrence rates of backscattered FAIs in equinox months, the lowest occurrence rates in June solstice, and the occurrence rates in three seasons all increasing with enhanced solar activity. For moderate and high solar activity conditions in equinox and December solstice, Figure 5(b)(c)(h)(i) shows that the initiation of backscattered FAIs mostly began after ~12:00 UT (~19:18 LT) and usually could persist into midnight or even extended to post-midnight sector. These FAIs initiated near the sunset hour

were usually freshly generated type echoes, still in the evolutionary phase, thus the echoes could grow to very high altitude, sometimes even exceeding the maximum of detectable altitude of the HCOPAR. The altitude of the FAIs usually kept declining as it went into the midnight and post-midnight sector, meaning that the FAIs occurred during this period were usually in the decay phase and were mostly continuation of post-sunset FAIs which drifted from outside of the FoV. This altitude-universal time distribution of FAIs occurrence rate is similar to the Sanya VHF radar observation during equinoctial months of 2012-2016 (Xie et al., 2018 and see Figure 2 in their paper). The Doppler velocities of post-midnight echoes were mostly negative (see Figure 3 in their paper), which reinforces our assertion that post-midnight FAIs in equinox over Hainan were mostly remnant structure of the pre-midnight echoes. In contrast, for high solar activity in June solstice, Figure 5(e)(f) shows that the altitude of the FAIs, which emerged near midnight or post-midnight sector, was much higher than other seasons and some of the FAIs echoes were still in the evolutionary phase, with the FAIs echoes keeping growing to high altitude after midnight. The evolutionary-type FAIs were sporadically observed near midnight in June solstice, despite the occurrence rate was very low. Under low solar flux condition, however, FAIs development were frequently observed in the post-midnight sector of June solstice by VHF radars in India and Indonesia (e.g., Patra et al., 2009, Otsuka et al., 2012, Nishioka et al., 2012, Ajith et al., 2015), as well as the C/NOFS and Swarm satellites (e.g., Yokoyama et al., 2011, Aa et al., 2020). Surprisingly, no increase of post-midnight FAIs occurrence has been observed by HCOPAR during the June solstice in low solar activity condition. Detailed discussion regarding this point is included in the following section. Moreover, the maximum altitude of the FAIs echoes was considerably lower for all three seasons during low solar activity condition than that during the

moderate and high solar activity conditions. Hence, solar activity level not only has a control on the FAIs occurrence rate, but also has an effect on the FAIs echoes maximum altitude.

3.1.2 Quiet-time F-region Vertical Plasma Drift Climatology

In order to better understand the dependence of the quiet-time FAIs occurrence rate and climatology variations on season and solar activity observed by the HCOPAR described above, we then analyzed the solar activity control on the F-region vertical plasma drift climatology for three seasons. Similarly, to exclude the possible geomagnetic disturbance effects, we only selected observations made when the daily mean kp index did not exceed 3. Figure 6 displays the daily curves of the averaged F-region vertical plasma drifts V_z (blue dotted line) that we obtained from measurements available from 2014-2017 under the quiet geomagnetic condition for different seasons and solar flux levels, in which grey error bars denote the standard deviations of the vertical plasma drifts. From top to bottom rows are the measurements for equinox, June solstice and December solstice and the first, second, third columns are the measurements for low, moderate and high solar activities, respectively. It can be seen in Figure 6 that the enhancement of the F-region evening vertical drifts before its reversal, known as PRE, usually occurred near sunset hours (09:00-12:00 UT/16:18-19:18 LT). For the sake of clearer comparison, the daily mean curves of V_z under low (blue), moderate (black) and high (red) solar activities are replotted in Figure 6(d)(h)(l) for three seasons. The vertical plasma drift during daytime did not show many differences for different seasons and solar activity levels, while the mean V_z near sunset hours was strongly affected by solar activity level. Among the three seasons, the increasing trend of the mean PRE with solar activity was most significant during equinox, with the peak mean PRE reaching 14 m/s when F10.7≥120 as shown in Figure 6(d). This can explain the highest

FAIs occurrence rate appeared in equinox months under high solar activity condition. Enhanced PRE activity uplifted the F-layer to higher altitude, providing a favorable condition for the R-T instability to grow, and thus boosted the FAIs occurrence rate in equinox. Comparing the results of equinox and December solstice in Figure 5 with the mean vertical plasma drift curve in Figure 6(d) and (l), the initial time of the majority of FAIs echoes was very close to the reversal time of V_z from positive to negative. It further demonstrates that the elevation of the F layer facilitated the rapid growth of the R-T instability, and when the F layer almost reached its peak height where v_{in} declined largely so that the R-T instability could become large enough to trigger the FAIs formation.

It has been well recognized that the vertical plasma drift is an important factor of the post-sunset plasma bubble generation (e.g. Huang, 2018a). As reported by many researchers, linear relationship between EPBs occurrence and equatorial vertical plasma drift has been verified by different instruments, such as CHAMP and ROCSAT-1 satellite observations (Stolle et al., 2008) and Jicamrca radar (Fejer et al., 1999). Because the vertical plasma drift around sunset hours due to PRE largely varies with solar activity (Fejer et al., 1979, Santos et al., 2013, Smith et al., 2016), the post-sunset EPBs occurrence rate thus is controlled by solar flux levels. Our results show that the quiet-time evening vertical plasma drift and FAIs occurrence climatology represented similar solar cycle and seasonal dependences. The higher occurrence rate of FAIs seen under higher solar activity condition can be attributed to the PRE dependence on the solar flux level. The seasonal occurrence rate of FAIs over Fuke can be well explained by the theory proposed by Tsunoda (1985). The magnetic declination angle over Fuke is close to 0° as shown in Figure 1, therefore, the solar terminator becomes more aligned with the magnetic meridian in

the equinox months. The small angle between the solar terminator and magnetic field flux tube leads to nearly simultaneous sunset at the conjugate E layers, making favorable conditions for the PRE development and for the growth of the R-T instability after sunset. Consequently, FAIs occurrence rate over Fuke usually peaks under high solar activity condition in equinox.

To further quantify the relationship of evening vertical plasma drift and FAIs occurrence at 110°E on a day-to-day basis for equinox, Figure 7 displayed the quiet-time solar cycle variations of the post-sunset peak PRE and the FAIs occurrence rate. The peak values of PRE were estimated from the maximum value of vertical plasma drift during 09-12 UT (16.3-19.3 LT) and were plotted as a function of the F10.7 index in Figure 7(a). We note that the magnitude of peak PRE displayed a positive correlation with F10.7 index for equinox, as indicated by the blue fitting curve in Figure 7(a). The mechanism of the PRE dependence on solar activity has been explained in terms of two factors, the thermospheric zonal wind and the longitudinal gradients of ionospheric conductivity at sunset time (e.g., Rishbeth, 1971; Heelis et al., 1974), both increasing with increasing solar flux. The red dots shown in Figure 7(a) marked the peak PRE and the corresponding F10.7 index of the quiet-time FAIs event days when the peak PRE was available. Note that peak PRE values are calculated by Digisonde measurements from above 300 km, thus its values can represent the actual vertical plasma drift. Figure 7(b) showed the FAIs occurrence rate variations as a function of the peak PRE for equinox, and the error bars represent the statistical discrepancy. Adopting the method of Huang and Hairston (2015), the FAIs occurrence rate is defined as the proportion of the FAIs events to the total events in each velocity bin of 5 m/s (e.g., 2.5 m/s$\leq V_z$<7.5 m/s and 7.5 m/s$\leq V_z$<12.5 m/s), ranging from -10 m/s to 70 m/s. The results show that the FAIs occurrence rates were zero when the peak PRE was less than 0 m/s,

and it raised rapidly as the magnitude of peak PRE increased and surpassed 0.5 when the peak PRE was larger than 20 m/s. The relationship between the FAIs occurrence rate and the peak PRE value is almost linear with a correlation coefficient reaching 0.97, as indicated by the black fitting curve in Figure 7(b). The threshold of peak PRE for definitive FAIs generation in equinox is ~30 m/s, which provides useful information for space weather forecast.

In June solstice, the mean vertical drift velocities remained positive, however, with large uncertainties, during 12-16 UT in the pre-midnight sector, so the day-to-day variations of V_z during this period could be large. This means that the F-layer might kept uplifting on certain days and thus could maintain the FAIs development in the midnight or even in the post-midnight sector. We then selected the days with evolutionary-type FAIs emerging after midnight in June solstice to calculate the average vertical drift and compared the result with that of the non-FAIs event days (i.e., the days before and after the event day). Figure 8 displays the mean V_z variations of the post-midnight FAIs event days (red) and non-FAIs days (black), in which error bars denote the standard deviations of the vertical drifts. The mean V_z during 13.5-15 UT on event days was larger than that on non-event days and the upper boundary of the red error bars during 13.5-15.5 UT was larger than the black error bars by ~5-13 m/s. Note that the drift data selected here is derived by measurement near and above 300 km, ensuring the Digisonde measurements coincide with the practical F-region vertical plasma drift. Hence, it is reasonable to infer that these post-midnight FAIs events were triggered due to the enhanced vertical plasma drift during the pre-midnight period.

However, the positive V_z in the pre-midnight sector does not always guarantee the FAIs development after midnight. As shown in Figure 6(h), the mean V_z during 12-16 UT in June solstice for F10.7<120 was larger than that for F10.7≥120, so it should have been more likely to detect higher FAIs occurrence rate in the midnight and post-midnight sector for lower solar activity condition during this season. As reported by many researchers, the post-midnight FAIs occurrence in Kototabang, Indonesia became more active in June solstice during solar minimum (e.g., Yokayama et al., 2011, Nishioka et al., 2012, Ajith et al., 2015), which is consistent with the average drift measurements. However, the results of the HCOPAR observations shown in Figure 5 were not consistent with the expectation based on the drift measurements. Considering the quiet-time vertical plasma drift climatology should be similar at the two nearby longitudes, the difference of post-midnight FAIs occurrence rate in June solstice during solar minimum years between Kototabang and Fuke should be caused by other factors. As reviewed by Otsuka (2018), the generation of quiet-time post-midnight FAIs can be explained by two mechanisms, i.e., the uplift of the F layer which may be related to midnight temperature maximums and the seeding of R-T instability by gravity waves propagating from below. Li et al. (2016) investigated the difference of EPBs occurrence rate between Sanya, China and Kototabang, Indonesia during September-October of 2012-2013 (near solar max), and found that the EPBs activity was more active at Kototabang due to a more active Intertropical Convergence Zone (ITCZ) situated around the longitude of Kototabang. We here conducted a similar study for June solstice during the low solar activity period of years 2014-2017. Figure 9 displays the outgoing long-wave radiation (OLR) variations during June solstice under low solar flux condition. The longitudinal and latitudinal variations of the daily mean OLR are shown in Figure 9a. It is obviously shown that the mean OLR values are smaller around the 100°E than that around 110°E. The smaller

values of OLR indicate deeper convection activity. As suggested by Gu and Zhang (2002) and Su et al. (2014), the thresholds of 205 and 190 can be used as good indicators for ITCZ activity that favors gravity wave occurrence. To further investigate the difference of ITCZ activity level between 100°E and 110°E, Figures 9b and 9c present the longitudinal and latitudinal variations of the occurrence rate of OLR (<205 and <190). The occurrence rates in each longitude versus latitude bin (2.5° ×2.5°) was calculated by the numbers of days with OLR < 205 and OLR < 190 in each bin divided by the total number of days. Considering that the gravity waves generated near magnetic equator act more efficiently in seeding the R-T instability (Tsunoda, 2010), the longitudinal variations of the averaged occurrence rates of OLR (<205) and OLR (<190) within ±5° magnetic latitude are presented in Figure 9d. It is clear that the occurrence rate of ITCZ activity is higher at the Kototabang longitude than that at the Fuke longitude. Thus, it is likely that the lower post-midnight FAIs occurrence rate at Fuke than Kototabang in June solstice of solar minimum years is a result of the longitudinal difference of ITCZ activity between 110°E and 100°E. Seeding sources from active ITCZ in June solstice may trigger the R-T instability to grow and the EPBs to develop after midnight at 100°E. Lacking seeding sources, even the vertical plasma drift velocity remained positive to maintain the elevation of the F layer in pre-midnight sector, it is much harder for the FAIs to develop after midnight at the Fuke site due to the much lower F-region bottom density gradient in the post-midnight sector than that in the post-sunset sector.

3.2. Magnetic Activity Dependence

To study the effect of magnetic activity on FAIs occurrence, we picked out the observational data of the HCOPAR during equinox months under high solar activity condition to analyze the

FAIs occurrence dependence on magnetic activity. The SYM-H and AE indices are used as the indicators of geomagnetic activity level. Considering that the effects of magnetic activity on the FAIs generation in the pre-midnight and post-midnight sectors can be different, due to the opposite polarization of the storm-time perturbation electric field, the statistical analysis is divided into two parts, i.e. pre-midnight and post-midnight sectors. Figure 10 illustrates the pre-midnight and post-midnight FAIs occurrence rate as a function of the SYM-H index. The first and second panels present the total minutes of available measurements and total minutes of FAIs events in different SYM-H bins. The third panel presents the normalized occurrence rate of FAIs in the corresponding SYM-H bins. Owing to the uneven time coverage of available observations in each SYM-H bin as shown in Figure 10(a), the error bars are added to the result of FAIs occurrence rate in Figure 10(c) to indicate possible statistical discrepancy, which can be calculated by the following equation:

$$\sigma = \sqrt{\frac{f \times (1-f)}{N-1}}, \tag{2}$$

where σ is the statistical discrepancy, f is the occurrence rate, and N is the total number of the statistical sample in each bin. The total minutes of available observation for SYM-H index lower than -60 nT are not shown in Figure 10(a), because no FAIs were detected when SYM-H is lower than -45 nT, as displayed in Figure 10(b). As depicted in Figure 10(c), the occurrence rates are obviously higher for the SYM-H index between -15 and 30 nT. Therefore, the FAIs events at the Fuke longitude in both pre-midnight and post-midnight sectors mainly occurred during non-storm time.

Figure 11 illustrates the pre-midnight and post-midnight FAIs occurrence rate under different auroral electrojet activity levels, i.e. low (0 nT<AE<100 nT), moderate (100 nT≤AE<400 nT)

and high ($AE \geq 400$ nT). The first and second panels show the total minutes of available measurements and total minutes of FAIs events in different AE bins. The third panel presents the normalized occurrence rate of FAIs in the corresponding AE bins. It is obvious that the normalized occurrence rate of FAIs decreases with increasing AE both in the pre-midnight and post-midnight sectors, which demonstrates that the FAIs occurrence was suppressed by enhanced auroral activities. As mentioned in the previous section, the post-midnight FAIs echoes in equinox almost confined to low altitudes, indicating that these echoes were mostly the remnant structure of post-sunset FAIs which migrated from elsewhere. Thus, the post-midnight FAIs occurrence showed a similar dependence on the SYM-H and AE indices with that of the pre-midnight FAIs. Under this circumstance, we then focus discussions on the post-sunset sector.

Numerous studies have demonstrated that geomagnetic storms can inhibit the generation of plasma bubble especially in the evening sector. Rastogi et al. (1981) found that the geomagnetic storms reduce the occurrence of scintillation at Huancayo during post-sunset hours. Based on data from ion drift meter aboard the Atmosphere Explorer E satellites, Singh et al. (1997) reported inhibition of spread F caused by increase in magnetic activity except near sunrise, where the plasma bubble activity has been found to increase with magnetic disturbance. By analyzing data from the polar-orbiting Dynamics Explorer 2 satellite, Palmroth et al. (2000) revealed that the generation of pre-midnight bubbles is suppressed by increasing magnetic activity, while in the morning side the probability of depletions increases with enhanced magnetic activity. In addition, Li et al. (2009) analyzed data from six ground-based GPS receivers in East Asia covering the period years 2001-2004 and found that magnetic activity appears to inhibit the EPBs generation with a time delay of 4-9 hours. The

suppression/promotion of plasma bubble generation depends on the disturbed electric field caused by geomagnetic disturbance in the equatorial ionosphere. In the post-sunset sector, dynamo electric field caused by disturbance neutral winds generated by enhanced Joule heating in the auroral zone (Blanc and Richmond, 1980) can lead to westward perturbation in the equatorial zonal electric field and downward vertical plasma drifts, which reduces the PRE and results in suppression of plasma bubble occurrence in post-sunset sector. Recently, based on 6 years ion of drift data measured by the C/NOFS satellite, Huang (2018b) verified that the suppression of EPBs during the post-sunset sector is related to the storm time DDEF. Sripathi et al. (2018) also studied the effect of storm time DDEF in suppressing the EPBs development over India during the 2 October 2013 geomagnetic storm. Similar to DDEF, the over-shielding electric field related with northward turning of the IMF Bz (Fujita et al., 2010) or substorm onsets (e.g., Hashimoto et al., 2011; Kikuchi et al., 2003; Wei et al., 2009) can also cause westward perturbation in the equatorial zonal electric field and downward vertical plasma drifts in evening sector thereby inhibiting the occurrence of plasma bubble.

To understand the underlying mechanism of auroral activities' control on post-sunset FAIs development, we compared the vertical plasma drift velocity in the dusk side for different auroral electrojet activity levels. The 5-min averaged AE index obtained from the OMNIWeb Data Explorer during 10-17 UT was used to calculate the mean level of auroral electrojet activity, that is, $\overline{\mathrm{AE}}_{(10\text{-}17\ \mathrm{UT})}$. As shown in Figure 12, the temporal variations of mean V_z during 08-17 UT for low (0 nT$< \overline{\mathrm{AE}}_{(10\text{-}17\ \mathrm{UT})} <$100 nT), moderate (100 nT$\leq \overline{\mathrm{AE}}_{(10\text{-}17\ \mathrm{UT})} <$400 nT) and high ($\overline{\mathrm{AE}}_{(10\text{-}17\ \mathrm{UT})} \geq$400 nT) auroral electrojet activity conditions are indicated by black, blue and red lines, respectively. The mean V_z during 10:00-12:00 UT (PRE period) obviously decreased with

increasing auroral activity level, with the evening peak mean V_z of 16.3 m/s, 13.0 m/s and 11.3 m/s for low, moderate and high auroral activity levels, respectively. Thus, the evening vertical plasma drift was weakened by enhanced auroral activity, especially when $\overline{\mathrm{AE}}_{(10\text{-}17\ \mathrm{UT})} \geq 400$ nT. The results demonstrate that enhanced geomagnetic activity can reduce the evening upward plasma drift, lower the R-T instability growth rate and is responsible for the suppression of the subsequent FAIs development in the dusk side. This suppression could be due to the modified thermospheric wind pattern during enhanced geomagnetic disturbances or could also be due to substorm related over-shielding electric fields.

4 Summary and Conclusions

Observations from a coherent scatter radar installed at Fuke and a nearby Digisonde installed at Sanya covering the period of 2014-2017 have been analyzed to statistically study the occurrence and characteristics of FAIs and vertical plasma drift climatology in terms of solar activity, season, and magnetic activity dependences. To construct the FAIs occurrence map as a function of universal time and season, we created the FAIs index as the metric of the FAIs occurrence. Daily measurement of the F-region plasma vertical drifts at the nearby location was used to derive the mean characteristics of plasma drifts and the PRE peak values under different solar activity, seasonal and magnetic activity conditions. The main findings of our investigation are summarized as follows:

1. The quiet-time behavior of the FAIs occurrence shows close relationship with the vertical plasma drift climatology. The mean evening vertical plasma drift, the peak PRE value and the FAIs occurrence rate peak during equinox months of high solar activity years and decrease

largely in solstice months of low solar activity years. The threshold of the peak PRE for definitive post-sunset FAIs generation is identified to be about 30 m/s for equinox. The relationship between the FAIs occurrence rate and the peak PRE value is almost linear, and the occurrence rate increases to 0.5 once the peak PRE value exceeds ~20 m/s. These quantitative findings provide valuable information for space weather forecast of the EPBs occurrence.

2. Different from Kototabang, i.e., a station at nearby longitude and in the southern hemisphere, the occurrence rate of the post-midnight FAIs in June solstice over Fuke did not increase with the decreasing F10.7 index. The difference of post-midnight FAIs occurrence rate in June solstice during low solar activity years between Fuke and Kototabang is suggested to be caused by the longitudinal difference of ITCZ activity. Since these two stations are only 10 degrees apart in longitude and at similar magnetic latitudes, this finding reveals the highly localized and dynamic nature of FAIs and EPBs, and exposes the challenges of related space weather forecast.

3. Enhanced geomagnetic activity based on SYM-H and AE indices tends to weaken the evening upward plasma drift and suppress the development of FAIs over Fuke in the post-sunset and post-midnight sectors. Modified thermospheric wind pattern during strong driving conditions and/or substorm-induced westward over-shielding electric field in the dusk side are considered to play a role in modulating the post-sunset upward plasma drift and inhibiting the FAIs development.

Acknowledgements

This work is supported by the National Natural Science Foundation of China, grant number 41627804. G. Chen acknowledges the support of the National Natural Science Foundation of China (41722404). H. Jin would like to acknowledge the China-Brazil Joint Laboratory for Space Weather (CBJLSW), National Space Science Center (NSSC), and the Chinese Academy of Sciences (CAS) for supporting her postdoctoral fellowship. The authors acknowledge the use of the HCOPAR data from the Chinese Meridian Project (http://data.meridianproject.ac.cn/). The solar F10.7 flux index, SYM-H index as well as AE index are obtained from the OMNIWeb Data Explorer (https://omniweb.gsfc.nasa.gov/). This publication makes use of data from Sanya Digisonde station, owned by Institute of Geology and Geophysics, Chinese Academy of Sciences (IGGCAS) and supported in part by Solar-Terrestrial Environment Research Network of CAS and Meridian Project of China. The Sanya Digisonde data can be obtained from the DriftBase of Global Ionospheric Radio Observatory (http://giro.uml.edu/). The daily mean interpolated OLR data can be accessed at the website of NOAA (https://psl.noaa.gov/data/gridded/data.interp_OLR.html#plot).

References

Aa, E., Zou, S., & Liu, S. (2020). Statistical analysis of equatorial plasma irregularities retrieved from Swarm 2013–2019 observations. Journal of Geophysical Research: Space Physics, 125, e2019JA027022. https://doi.org/10.1029/2019JA027022

Aa, E., Zou, S., Ridley, A. J., Zhang, S.-R., Coster, A. J., Erickson, P. J., et al. (2019). Merging of storm time midlatitude traveling ionospheric disturbances and equatorial plasma bubbles. Space Weather, 17, 285–298. https://doi.org/10.1029/2018SW002101

Aa, E., Huang, W., Liu, S., Ridley, A., Zou, S., Shi, L., … & Wang, T. (2018). Midlatitude plasma bubbles over China and adjacent areas during a magnetic storm on 8 September 2017. Space Weather, 16, 321–331. https://doi.org/10.1002/2017SW001776

Abdu, M. A. (2012). Equatorial spread F/plasma bubble irregularities under storm time disturbance electric fields. Journal of Atmospheric and Solar: Terrestrial Physics, 75, 44–56.

Ajith, K. K., S. T. Ram, M. Yamamoto, T. Yokoyama, V. S. Gowtam, Y. Otsuka, T. Tsugawa, and K. Niranjan (2015), Explicit characteristics of evolutionary-type plasma bubbles observed from Equatorial Atmosphere Radar during the low to moderate solar activity years 2010–2012, J. Geophys. Res. Space Physics, 120, 1371–1382, doi:10.1002/2014JA020878.

Basu, S., Groves, K. M., Basu, S., & Sultan, P. J. (2002). Specification and forecasting of scintillations in communication/navigation links: current status and future plans. Journal of atmospheric and solar-terrestrial physics, 64(16), 1745-1754.

Basu, S., E. MacKenzie, & S. Basu (1988), Ionospheric constraints on VHF/UHF communication links during solar maximum and minimum periods, Radio Sci., 23, 363–378, doi:10.1029/RS023i003p00363.

Bertoni, F., Batista, I. S., Abdu, M. A., Reinisch, B. W., & Kherani, E. A. (2006). A comparison of ionospheric vertical drift velocities measured by Digisonde and Incoherent Scatter Radar at the magnetic equator. Journal of atmospheric and solar-terrestrial physics, 68(6), 669-678.

Blanc, M., & Richmond, A. D. (1980). The ionospheric disturbance dynamo. Journal of Geophysical Research, 85(A4), 1669–1688. https://doi.org/10.1029/JA085iA04p01669

Burke, W. J., C. Y. Huang, L. C. Gentile, & L. Bauer (2004a), Seasonal-longitudinal variability of equatorial plasma bubble occurrence, Ann. Geophys., 22, 3089.

Burke, W. J., L. C. Gentile, C. Y. Huang, C. E. Valladares, & S. Y. Su (2004b), Longitudinal variability of equatorial plasma bubbles observed by DMSP and ROCSAT-1, J. Geophys. Res., 109, A12301, doi:10.1029/2004JA010583.

Carter, B. A., K. Zhang, R. Norman, V. V. Kumar, & S. Kumar (2013), On the occurrence of equatorial F-region irregularities during solar minimum using radio occultation measurements, J. Geophys. Res. Space Physics, 118, 892–904, doi:10.1002/jgra.50089.

Chen, G., Jin, H., Yan, J., Cui, X., Zhang, S., Yan, C., et al. (2017). Hainan Coherent Scatter Phased Array Radar (HCOPAR): System design and ionospheric irregularity observations. IEEE Transactions on Geoscience and Remote Sensing, 55(8), 4757–4765.

Fejer, B. G., L. Scherliess, & E. R. dePaula (1999), Effects of the vertical plasma drift velocity on the generation and evolution of equatorial spread F, J. Geophys. Res., 104(A9), 19859–19869, doi: 10.1029/1999JA900271.

Fejer, B., D. Farley, R. Woodman, & C. Calderon (1979), Dependence of equatorial F region vertical drifts on season and solar cycle, J. Geophys. Res., 84(A10), 5792–5796, doi: 10.1029/JA084iA10p05792.

Fujita, S., Kikuchi, T., & Tanaka, T. (2010). State transition of the magnetosphere-ionosphere compound system due to a northward turn of the interplanetary magnetic field revealed from a global magnetohydrodynamic simulation and formation of the overshielding potential. Journal of Geophysical Research, 115, A11210, doi: 10.1029/2010JA015550.

Gu, G., & C. Zhang (2002), Cloud components of the Intertropical Convergence Zone, J. Geophys. Res., 107(D21), 4565, doi:10.1029/2002JD002089.

Hashimoto, K. K., Kikuchi, T., Watari, S., & Abdu, M. A. (2011). Polar-equatorial ionospheric currents driven by the region 2 field-aligned currents at the onset of substorms. Journal of Geophysical Research, 116, A0921. https://doi.org/10.1029/2011JA016442

Heelis, R. A., Kendall, P. C., Moffet, R. J., Windle, D. W., & Rishbeth, H. (1974). Electrical coupling of the E- and F- region and its effects on the F-region drifts and winds, Planet. Space Sci., 22(5), 743–756.

Hu, L., Zhao, X., Sun, W., Wu, Z., Zheng, J., Xie, H., et al. (2020). Statistical characteristics and correlation of low-latitude F region bottom-type irregularity layers and plasma plumes over Sanya. Journal of Geophysical Research: Space Physics, 125, e2020JA027855. https://doi.org/10.1029/2020JA027855

Huang, C.-S. (2018a). Effects of the postsunset vertical plasma drift on the generation of equatorial spread F. Progress in Earth and Planetary Science, 5(1), 3. https://doi.org/10.1186/s40645-017-0155-4

Huang, C.-S. (2018b). Effects of geomagnetic storms on the postsunset vertical plasma drift in the equatorial ionosphere. Journal of Geophysical Research: Space Physics, 123, 4181-4191. https://doi.org/10.1029/2018JA025360

Huang, C.-S., and Hairston, M. R. (2015). The postsunset vertical plasma drift and its effects on the generation of equatorial plasma bubbles observed by the C/ NOFS satellite, J. Geophys. Res. Space Physics, 120,2263–2275, doi:10.1002/2014JA020735.

Huang, C. Y., W. J. Burke, J. S. Machuzak, L. C. Gentile, & P. J. Sultan (2001), DMSP observations of equatorial plasma bubbles in the topside ionosphere near solar maximum, J. Geophys. Res., 106, 8131–8142, doi:10.1029/2000JA000319.

Jin, H., Zou, S., Chen, G., Yan, C., Zhang, S., & Yang, G. (2018). Formation and evolution of low-latitude F region field-aligned irregularities during the 7–8 September 2017 storm: Hainan coherent scatter phased array radar and digisonde observations. Space Weather, 16, 648–659. https://doi.org/10.1029/2018SW001865

Kelley, M. C. (1989). The Earth's ionosphere, Int. Geophys. Ser., vol. 43, Elsevier, New York.

Kikuchi, T., Hashimoto, K. K., Kitamura, T.-I., Tachihara, H., & Fejer, B. (2003). Equatorial counterelectrojets during substorms. Journal of Geophysical Research, 108(A11), 1406. https://doi.org/10.1029/2003JA009915

Kumar, S., W. Chen, Z. Liu, & S. Ji (2016), Effects of solar and geomagnetic activity on the occurrence of equatorial plasma bubbles over Hong Kong, J. Geophys. Res. Space Physics, 121, 9164–9178, doi:10.1002/2016JA022873.

Li, G., Otsuka, Y., Ning, B., Abdu, M. A., Yamamoto, M., Wan, W., Liu, L. & Abadi, P. (2016). Enhanced ionospheric plasma bubble generation in more active ITCZ, Geophys. Res. Lett., 43, 2389–2395, doi:10.1002/2016GL068145.

Li, G., Ning, B., Liu, L., Wan, W., & Liu, J. Y. (2009). Effect of magnetic activity on plasma bubbles over equatorial and low-latitude regions in East Asia. Ann. Geophys, 27, 303-312.

Martinis, C. R., Mendillo, M. J., & Aarons, J. (2005). Toward a synthesis of equatorial spread F onset and suppression during geomagnetic storms. Journal of Geophysical Research, 110, A07306. https://doi.org/10.1029/2003JA010362

Nishida, A. (1968). Coherence of geomagnetic DP 2 fluctuations with interplanetary magnetic variations. Journal of Geophysical Research, 73(17), 5549–5559. https://doi.org/10.1029/JA073i017p05549

Nishioka, M., Y. Otsuka, K. Shiokawa, T. Tsugawa, Effendy, P. Supnithi, T. Nagatsuma, & K. T. Murata (2012), On post-midnight field-aligned irregularities observed with a 30.8-MHz radar at a low latitude: Comparison with F-layer altitude near the geomagnetic equator, J. Geophys. Res., 117, A08337, doi:10.1029/2012JA017692.

Okoh, D., Rabiu, B., Shiokawa, K., Otsuka, Y., Segun, B., Falayi, E., ⋯ Kaka, R. (2017). First study on the occurrence frequency of equatorial plasma bubbles over West Africa using an all‐sky airglow imager and GNSS receivers. Journal of Geophysical Research: Space Physics, 122, 12,430–12,444. https://doi.org/10.1002/2017JA024602

Otsuka, Y. (2018). Review of the generation mechanisms of post-midnight irregularities in the equatorial and low-latitude ionosphere. Prog Earth Planet Sci 5, 57. https://doi.org/10.1186/s40645-018-0212-7

Otsuka, Y., Shiokawa, K., Nishioka, M., & Effendy. (2012). VHF radar observations of post-midnight F-region field-aligned irregularities over Indonesia during solar minimum, Indian J Radio Space Phys (IJRSP), 41, 199–207

Ott, E. (1978). Theory of Rayleigh-Taylor bubbles in the equatorial ionosphere. Journal of Geophysical Research, 83(A5), 2066.

Palmroth, M., Laakso, H., Fejer, B. G., & Pfaff, R. F. Jr. (2000). DE 2 observations of morningside and eveningside plasma density depletions in the equatorial ionosphere. Journal of Geophysical Research, 105(A8), 18,429-18,442. https://doi.org/10.1029/1999JA005090

Patra, A. K., Phanikumar, D. V., & Pant, T. K. (2009). Gadanki radar observations of F region field-aligned irregularities during June solstice of solar minimum: first results and

preliminary analysis. J Geophys Res 114: A12305. https://doi.org/10.1029/2009JA014437

Rastogi, R. G., Mullen, J. P., & MacKenzie, E. (1981). Effect of geomagnetic activity on equatorial radio VHF scintillations and spread F. Journal of Geophysical Research, 86(A5), 3661-3664. https://doi.org/10.1029/JA086iA05p03661

Reinisch, B. W., Galkin, I. A., Khmyrov, G. M., Kozlov, A. V., Bibl, K., Lisysyan, I. A., et al. (2009). New Digisonde for research and monitoring applications. Radio Science, 44, RS0A24. https://doi.org/10.1029/2008RS004115

Rishbeth, H. (1971), Polarization fields produced by winds in the equatorial F region, Planet. Space Sci., 19, 357–369.

Santos, A. M., M. A. Abdu, J. H. A. Sobral, M. Mascarenhas, & P. A. B. Nogueira (2013), Equatorial evening prereversal vertical drift dependence on solar EUV flux and F10.7 index during quiet and disturbed periods over Brazil, J. Geophys. Res. Space Physics, 118, 4662–4671, doi:10.1002/jgra.50438.

Shi, J. K., G. J. Wang, B. W. Reinisch, S. P. Shang, X. Wang, G. Zherebotsov, & A. Potekhin (2011), Relationship between strong range spread F and ionospheric scintillations observed in Hainan from 2003 to 2007, J. Geophys. Res., 116, A08306, doi:10.1029/2011JA016806.

Singh, S., Bamgboye, D. K., McClure, J. P., & Johnson, F. S. (1997). Morphology of equatorial plasma bubbles. Journal of Geophysical Research,102(A9), 20,019–20,029. https://doi.org/10.1029/97JA01724

Smith, J. M., F. S. Rodrigues, B. G. Fejer, & M. A. Milla (2016), Coherent and incoherent scatter radar study of the climatology and day-to-day variability of mean F region vertical drifts

and equatorial spread F, J. Geophys. Res. Space Physics, 121, 1466–1482, doi:10.1002/2015JA021934.

Sripathi, S., Banola, S., Emperumal, K., Suneel Kumar, B., & Radicella, S. M. (2018). The role of storm time electrodynamics in suppressing the equatorial plasma bubble development in the recovery phase of a geomagnetic storm. Journal of Geophysical Research: Space Physics, 123, 2336–2350. https://doi.org/10.1002/2017JA024956

Stolle, C., Lühr, H., & Fejer, B. G. (2008). Relation between the occurrence rate of ESF and the equatorial vertical plasma drift velocity at sunset derived from global observations. Ann. Geophys, 26, 3979-3988.

Su, S.-Y., C. Wu, & C. Liu (2014), Correlation between the global occurrences of ionospheric irregularities and deep atmospheric convective clouds in the Intertropical Convergence Zone (ITCZ), Earth Planets Space, 66, 134.

Su, S.-Y., C. K. Chao, & C. H. Liu (2008), On monthly/seasonal/longitudinal variations of equatorial irregularity occurrences and their relationship with the postsunset vertical drift velocities, J. Geophys. Res., 113, A05307, doi:10.1029/2007JA012809.

Tsunoda, R. T. (2010), On seeding equatorial spread F during solstices, Geophys. Res. Lett., 37, L05102, doi:10.1029/2010GL042576.

Tsunoda, R. T. (1985), Control of the seasonal and longitudinal occurrence of equatorial scintillations by the longitudinal gradient in integrated E region Pedersen conductivity, J. Geophys. Res., 90, 447–456.

Tulasi Ram, S., P. V. S. Rama Rao, D. S. V. V. D. Prasad, K. Niranjan, S. Gopi Krishna, R. Sridharan, & S. Ravindran (2008), Local time dependent response of postsunset ESF during geomagnetic storms, J. Geophys. Res., 113, A07310, doi:10.1029/2007JA012922.

Wan, X., Xiong, C., Rodriguez-Zuluaga, J., Kervalishvili, G. N., Stolle, C., & Wang, H. (2018). Climatology of the occurrence rate and amplitudes of local time distinguished equatorial plasma depletions observed by Swarm satellite. Journal of Geophysical Research: Space Physics, 123, 3014–3026. https://doi.org/10.1002/2017JA025072

Wang, C. (2010), New chains of space weather monitoring stations in China, Space Weather, 8, S08001, doi:10.1029/2010SW000603.

Wei, Y., Pu, Z., Hong, M., Zong, Q., Ren, Z., Fu, S., et al. (2009). Westward ionospheric electric field perturbations on the dayside associated with substorm processes. Journal of Geophysical Research, 114, A12209. https://doi.org/10.1029/2009JA014445

Xie, H., Li, G., Zhao, X., Hu, L., Wu, B., & Ning, B. (2018). Statistical study on the occurrences of postsunset ionospheric E, valley, and F region irregularities and their correlations over low-latitude Sanya. Journal of Geophysical Research: Space Physics, 123, 9873–9880. https://doi.org/10.1029/2018JA025729

Yizengaw, E., & Groves, K. M. (2018). Longitudinal and seasonal variability of equatorial ionospheric irregularities and electrodynamics. Space Weather, 16, 946–968. https://doi.org/10.1029/2018SW001980

Yokoyama, T., Pfaff, R. F., Roddy, P. A., Yamamoto, M., & Otsuka, Y. (2011). On postmidnight low-latitude ionospheric irregularities during solar minimum: 2. C/NOFS observations and comparisons with the Equatorial Atmosphere Radar. Journal of Geophysical Research, 116, A11326. https://doi.org/10.1029/2011JA016798

Zhan, W., Rodrigues, F., & Milla, M. (2018). On the genesis of postmidnight equatorial spread F: Results for the American/Peruvian sector. Geophysical Research Letters, 45, 7354–7361.https://doi.org/10.1029/2018GL078822

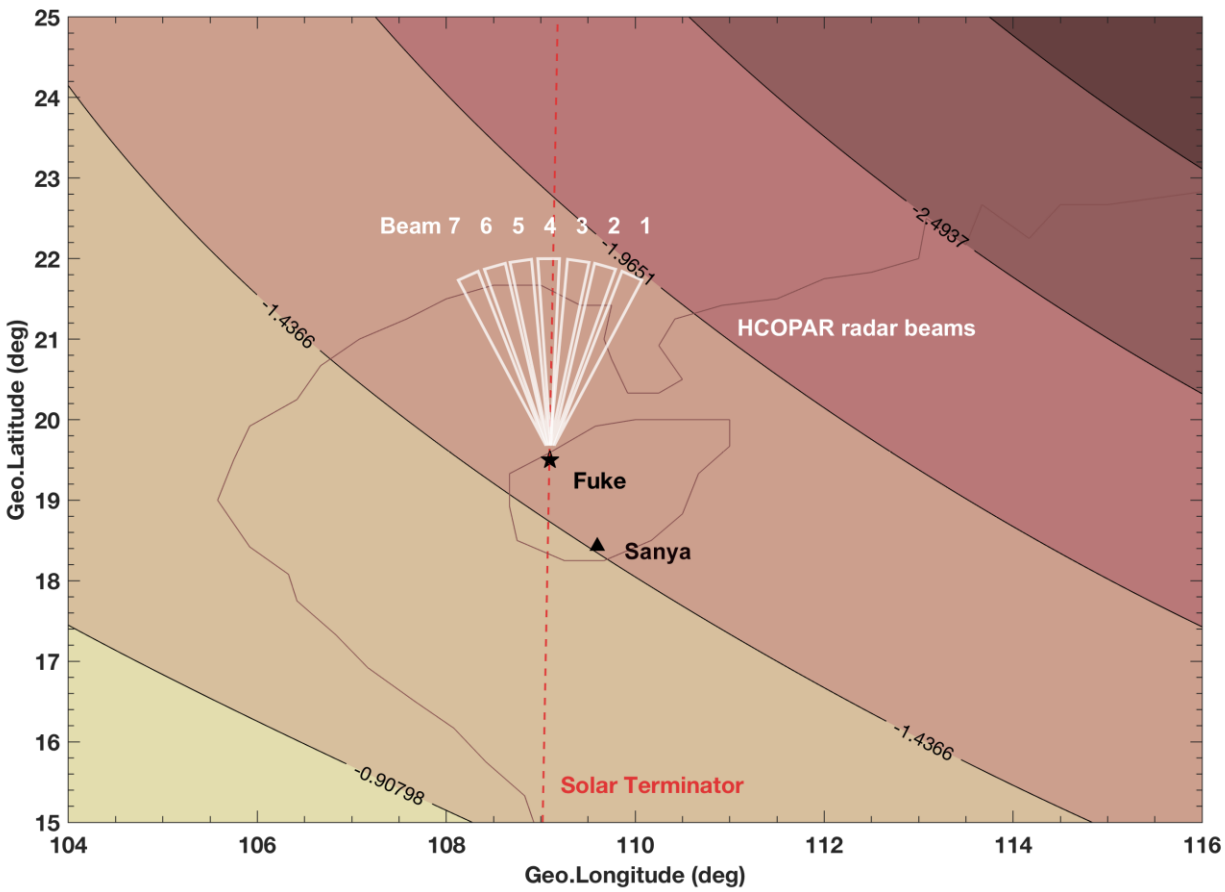

Figure 1. Map projection of the seven beam directions of the HCOPAR. The locations of Fuke and Sanya are marked with black star and triangle, respectively. Filled contours represent the magnetic field declination near the radar site. The red dashed line indicates the solar terminator at the sunset time over Fuke at the March equinox in 2014.

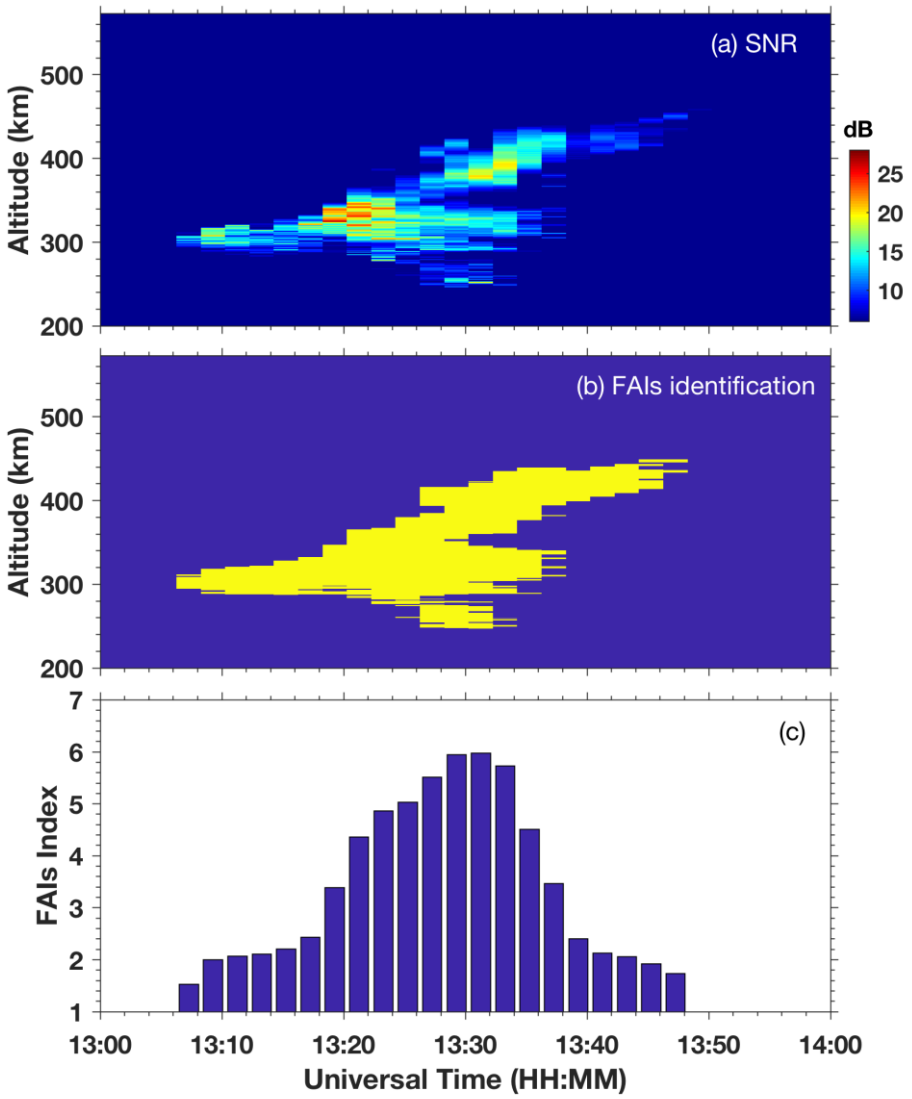

Figure 2. An example of FAIs measurement on 24 February 2014. (a) Local time and altitude variations of FAIs echo signal-to-noise ratio (dB), (b) FAIs identification by setting a threshold of SNR larger than 5 dB (yellow/blue indicates the occurrence/non-occurrence of FAIs, respectively), (c) FAIs index (see text for explanation) as a function of universal time.

Figure 3. (a-d) Universal time and seasonal variations in the FAIs index (see text for explanation) observed by the HCOPAR from 2014 to 2017. FAIs index ≥1 was regarded as echoes from FAIs.

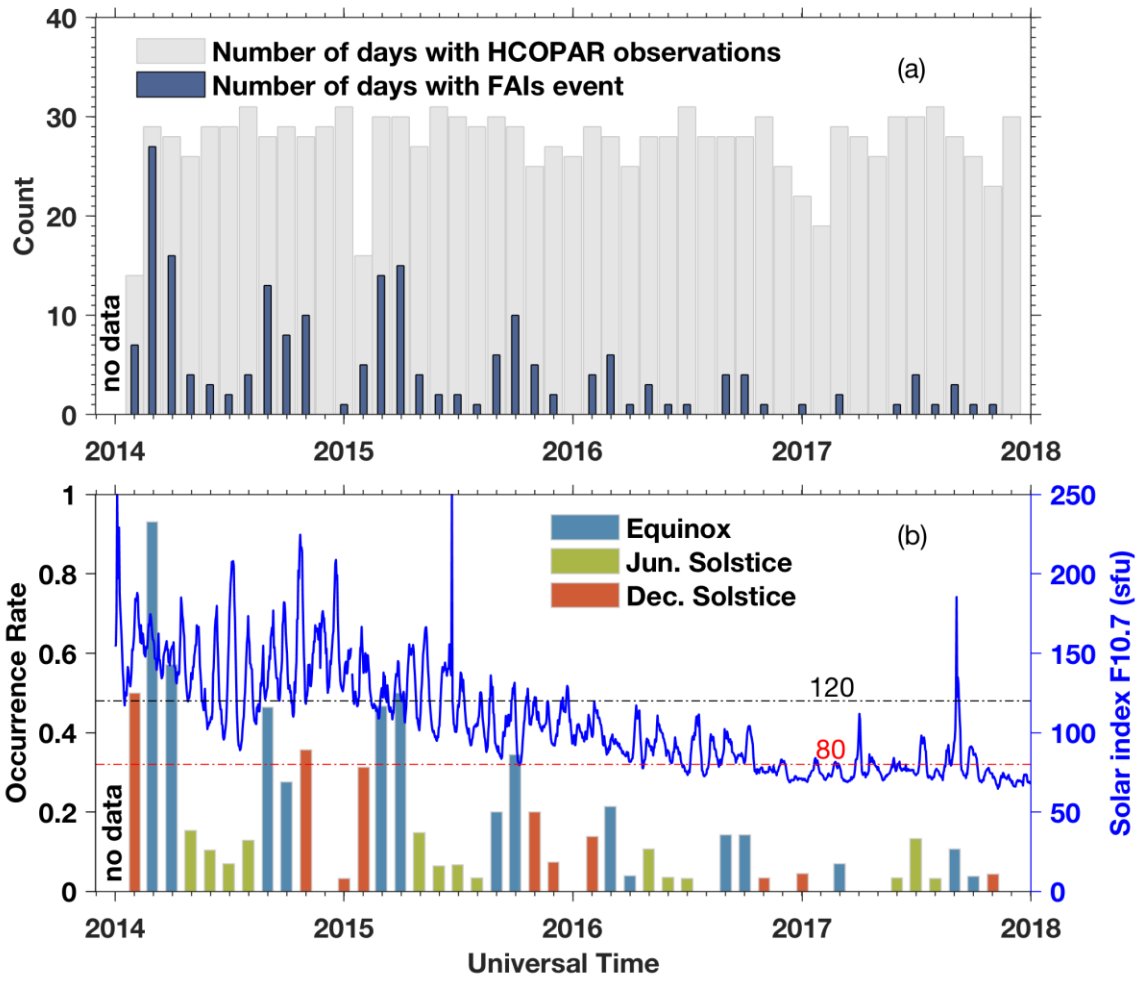

Figure 4. (a) Histogram showing the monthly day numbers of HCOPAR observations and FAIs event over Fuke during 2014-2017. The grey bars represent the number of days with measurements by the HCOPAR and the blue bars represent the number of days with FAIs observed by the HCOPAR in each month. (b) The normalized FAIs occurrence rate in each month during 2014-2017. The light blue, light green and orange bars indicate the FAIs occurrence rate for equinox, June solstice and December solstice, respectively. The temporal variation of daily-averaged F10.7 solar radio flux from 2014 to 2017 is also plotted. The black and red dashed lines mark the critical value of 80 and 120 for solar activity level, respectively.

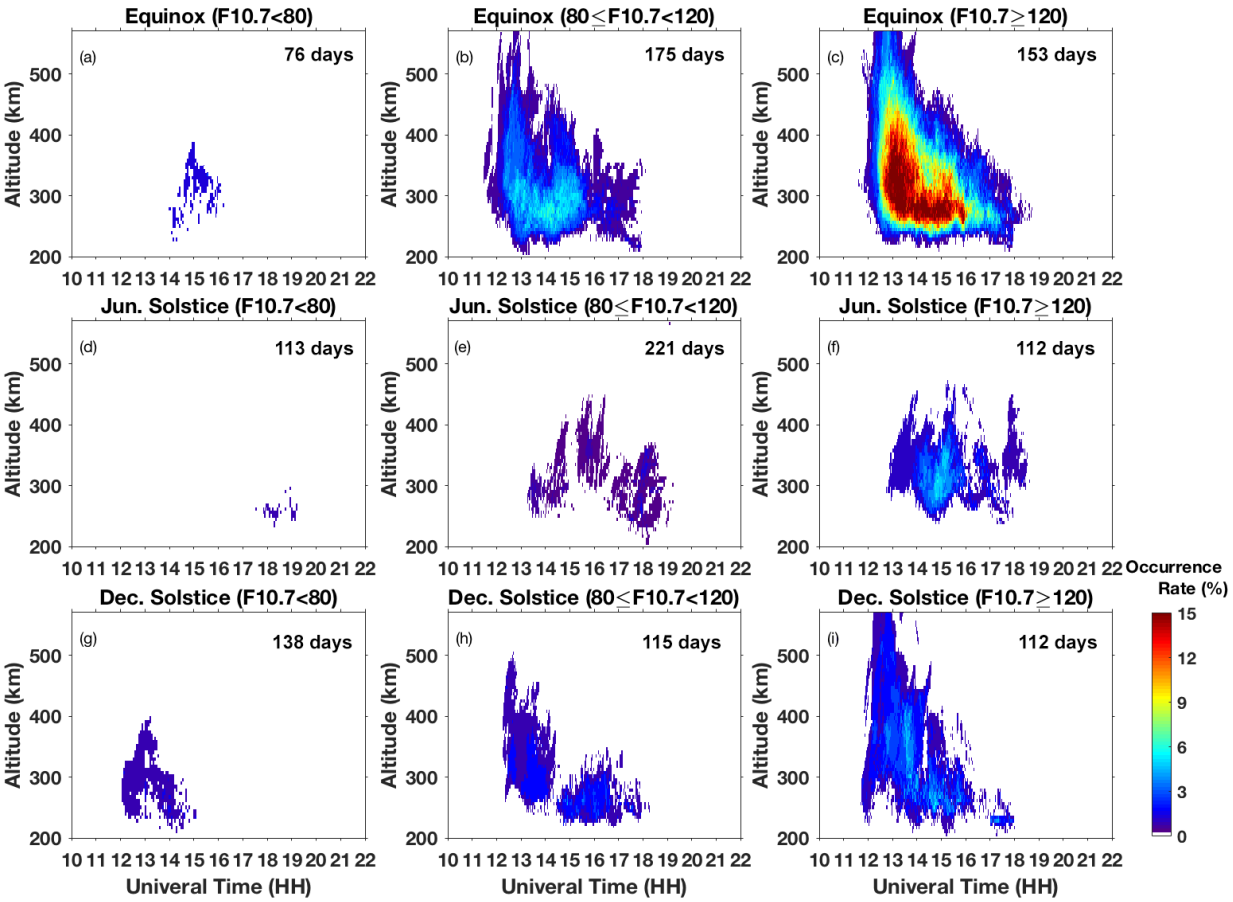

Figure 5. Color-coded occurrence rate of quiet-time F-region FAIs observed by the HCOPAR during 2014-2017 as a function of universal time and altitude. Each panel shows a season and solar activity level. The number of the days when the HCOPAR observations are available for each panel is mentioned. From top to bottom rows are measurements for equinox, June solstice and December solstice and the left, middle and right columns are measurements for low, moderate and high solar activities, respectively.

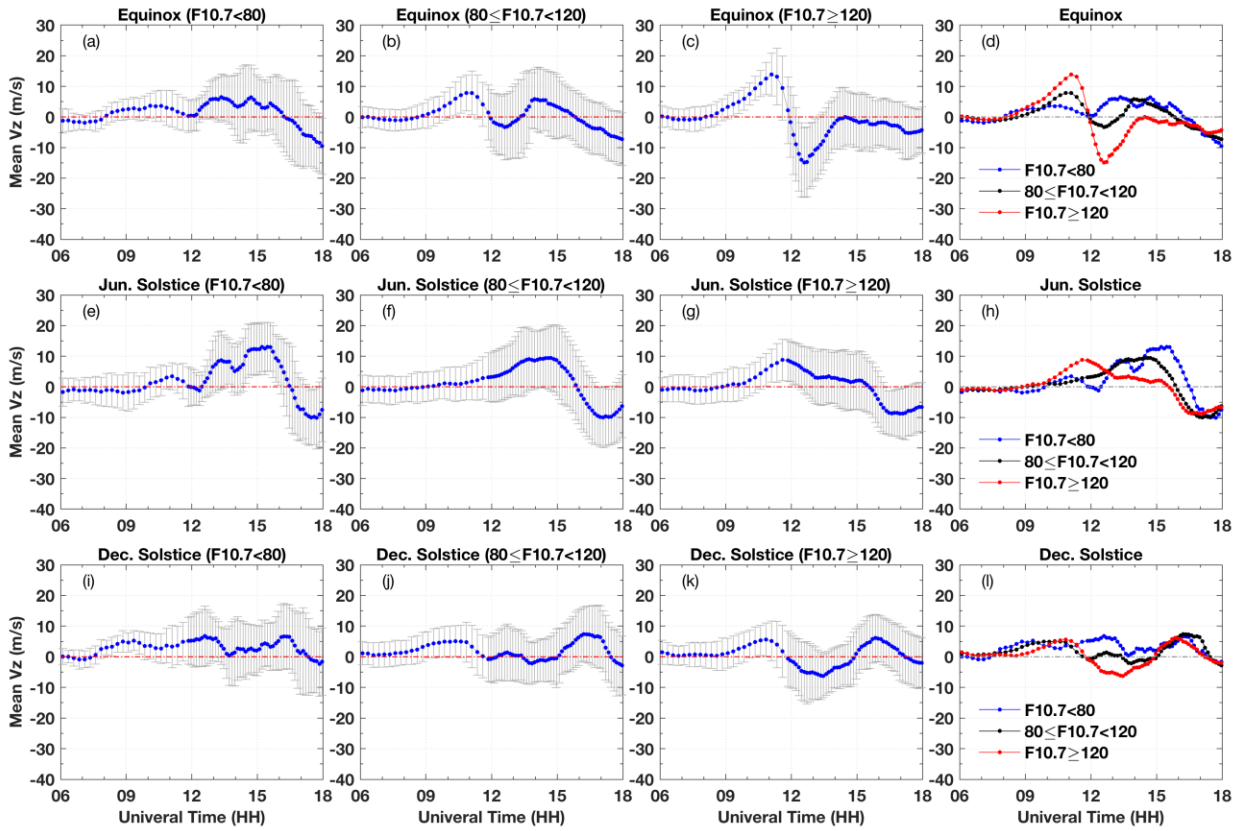

Figure 6. Quiet-time F-region mean vertical drift velocity (mean V_z, blue dotted lines) as a function of universal time. The grey error bars denote the standard deviations of the vertical plasma drifts. Each panel represents a season and solar activity level. From top to bottom rows are measurements for equinox, June solstice and December solstice and the first, second and third columns are measurements for low, moderate and high solar activities, respectively. The mean V_z curves for three solar flux conditions are merged in the fourth column. The red, black and blue dotted lines represent the mean V_z of high, moderate and low solar flux conditions, respectively.

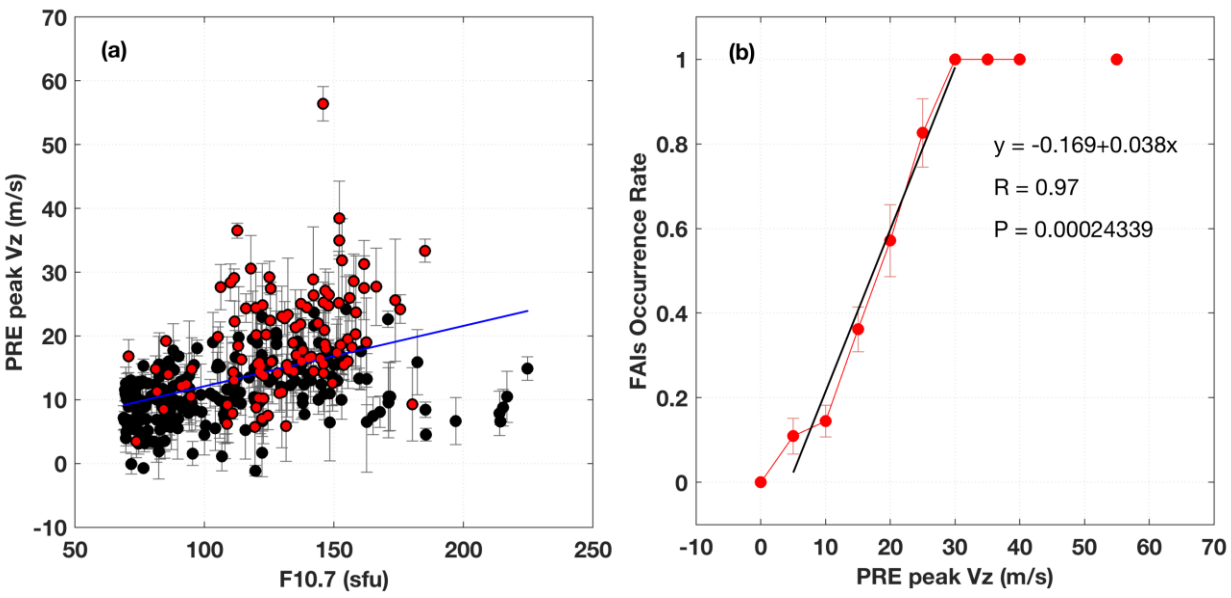

Figure 7. (a) Scatterplots showing the quiet-time post-sunset PRE peak V_z as a function of F10.7 index for equinox. The red dots indicate the peak PRE and the corresponding F10.7 index of the quiet-time FAIs event days when peak PRE was available. (b) FAIs occurrence rate versus PRE peak V_z for equinox.

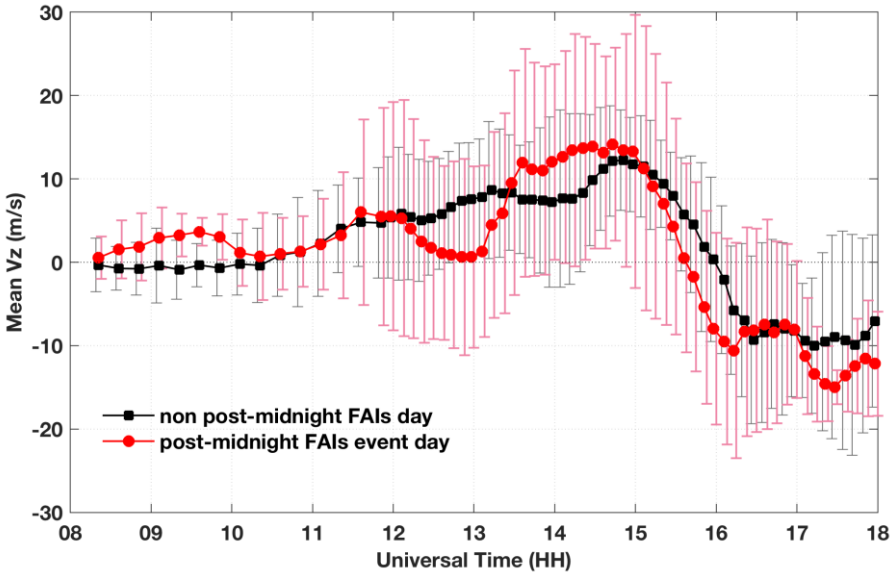

Figure 8. Mean V_z variations of post-midnight FAIs event days (red) and non-FAIs event days (black) as a function of universal time. Error bars represent the standard deviations of the vertical plasma drifts.

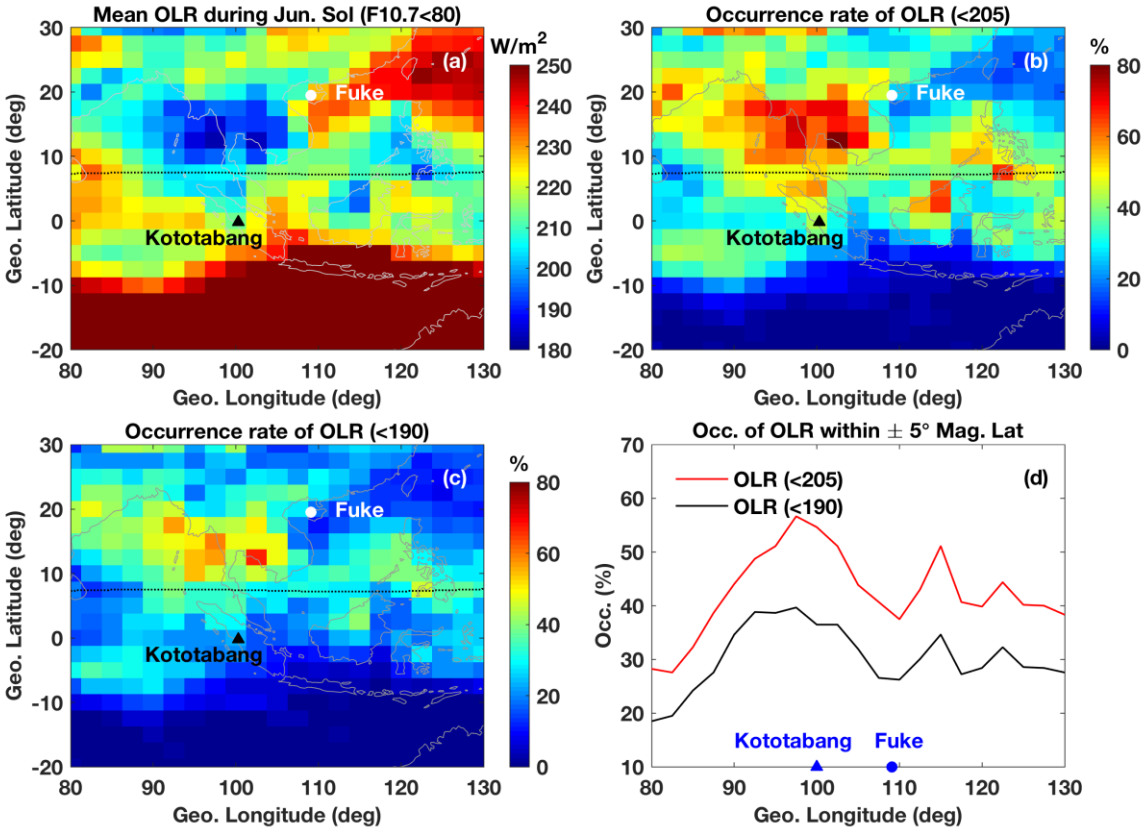

Figure 9. The longitudinal and latitudinal variations of (a) mean outgoing long-wave radiation (OLR) during June solstice under low solar activity condition, (b) occurrence rate of OLR (<205) and (c) occurrence rate of OLR (<190). The black dashed lines indicate the location of the magnetic equator. (d) The averaged occurrence rates of OLR (<205 and <190) within $\pm 5°$ magnetic latitude as a function of longitude. The locations of Kototabang and Fuke are indicated by triangles and dots, respectively.

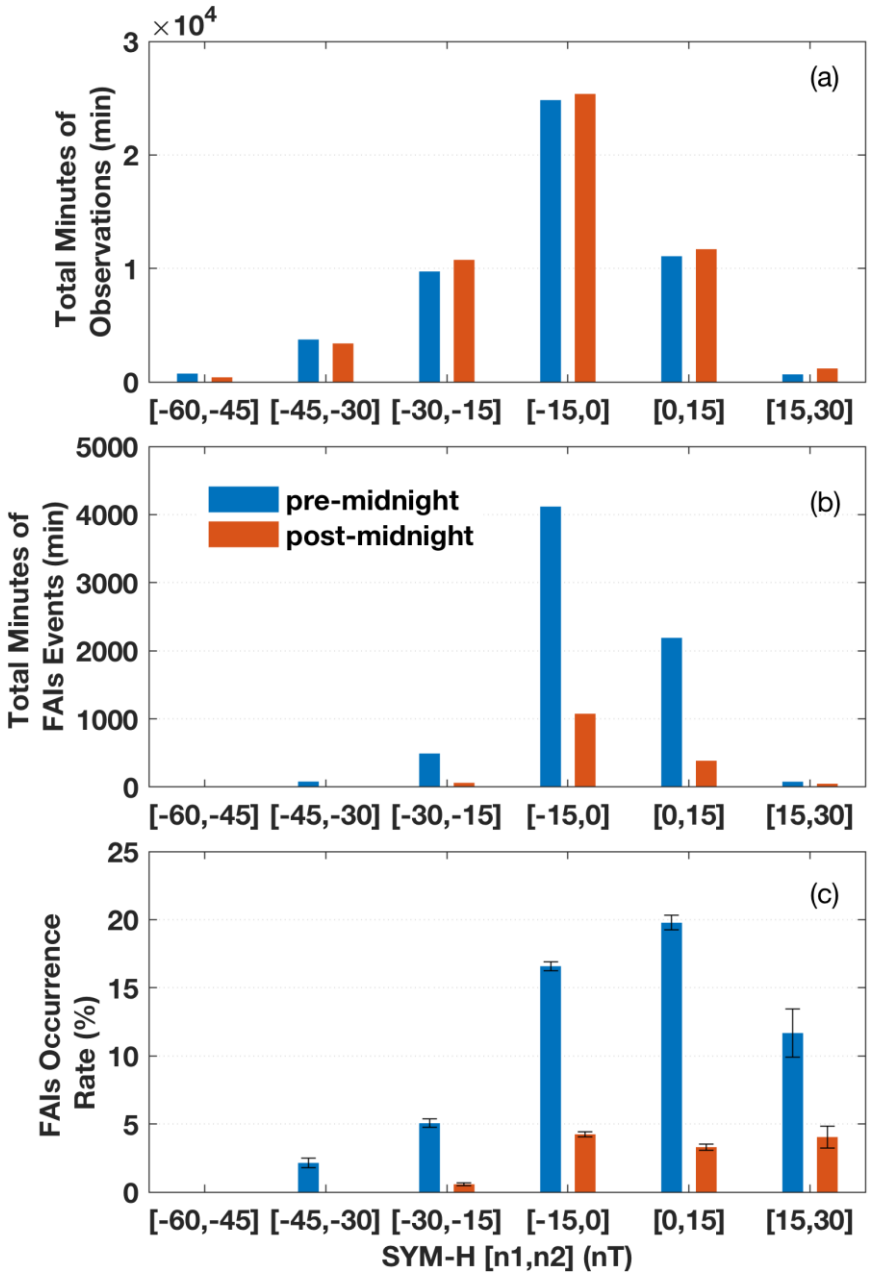

Figure 10. (a) Total minutes of available observations from the HCOPAR as a function of SYM-H index, (b) Total minutes of FAIs events observed by the HCOPAR as a function of SYM-H index, (c) Normalized FAIs occurrence rate observed by the HCOPAR as a function of SYM-H index. Blue/orange bars present the results in pre-midnight/post-midnight sector. The error bars in (c) illustrate the statistical bias due to the sample size.

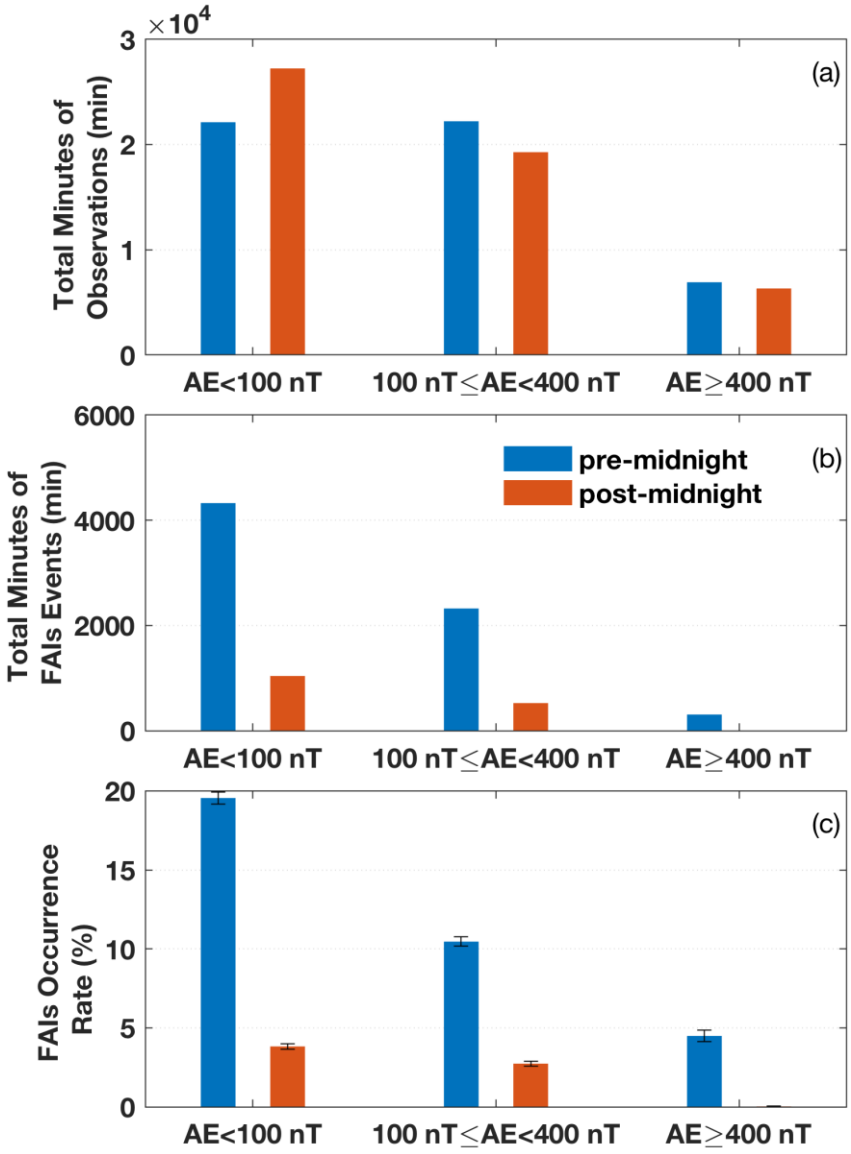

Figure 11. (a) Total minutes of available observations from the HCOPAR as a function of AE index, (b) Total minutes of FAIs events observed by the HCOPAR as a function of AE index, (c) Normalized FAIs occurrence rate observed by the HCOPAR as a function of AE index. Blue/orange bars present the results in pre-midnight/post-midnight sector. The error bars in (c) illustrate the statistical bias due to the sample size.

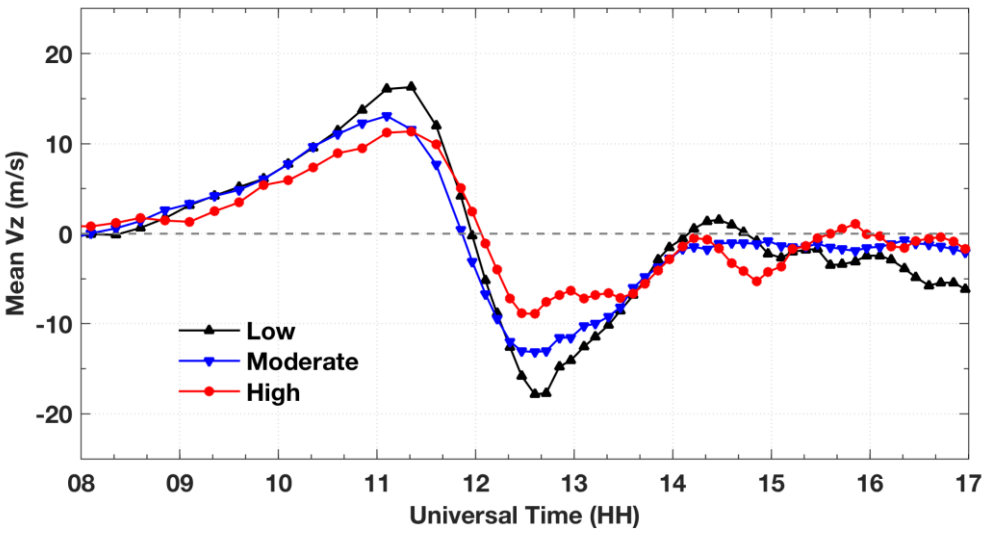

Figure 12. Mean V_z variations as a function of universal time for different auroral activity levels. The black, blue and red lines represent low, moderate and high auroral activity levels, respectively.